



Original paper



The compact line-focus X-ray tube for microbeam radiation therapy — Focal spot characterisation and collimator design

Christian Petrich^{a,b,c,d} *,¹, Johanna Winter^{b,c,d} , Anton Dimroth^{d,e}, Jan J. Wilkens^{a,b} , Stefan Bartzsch^{b,c,d}

^a TUM School of Natural Sciences, Technical University of Munich (TUM), Garching, Germany

^b Department of Radiation Oncology, TUM School of Medicine and Health and Klinikum rechts der Isar, TUM University Hospital, Technical University of Munich (TUM), Munich, Germany

^c Institute of Radiation Medicine, Helmholtz Zentrum München GmbH, German Research Center for Environmental Health, Neuherberg, Germany

^d Forschungs-Neutronenquelle Heinz Maier-Leibnitz Zentrum (FRM II), Technical University of Munich (TUM), Garching, Germany

^e Central Institute for Engineering, Electronics and Analytics (ZEA-1), Forschungszentrum Jülich GmbH, Jülich, Germany

ARTICLE INFO

Keywords:

Microbeam radiation therapy
Line-focus X-ray tube
Focal spot visualisation
Multislit collimator
Monte Carlo simulations

ABSTRACT

Purpose: Microbeam radiation therapy (MRT) has shown superior healthy tissue sparing at equal tumour control probabilities compared to conventional radiation therapy in many preclinical studies. The limitation to preclinical research arises from a lack of suitable radiation sources for clinical application of MRT due to high demands on beam quality. To overcome these limitations, we developed and built the first prototype of a line-focus X-ray tube (LFXT). During commissioning, characterisation of the X-ray focal spot is necessary. For the generation of microbeams, we require a specially designed collimator adapted to the LFXT.

Methods: We present an adapted edge method and a pinhole method for focal spot measurements of the LFXT prototype as well as the design of the microbeam collimator with a slit width of 50 μm , spaced by 400 μm . Monte Carlo simulations validated the focal spot measurement techniques and the design of the collimator.

Results: We showed that the adapted edge method is more complex but superior to the adapted pinhole method in terms of quantitative validity. Simulations for the microbeam collimator showed a sharp microbeam dose profile with a peak-to-valley dose ratio (PVDR) above 23 throughout 50 mm of water.

Conclusion: During commissioning, the adapted focal spot visualisation methods will be used to determine the focal spot dimensions and to optimise machine parameters. The LFXT prototype will enable preclinical MRT with significantly higher dose rates than any other compact MRT source and will pave the way for the first clinical trials in a hospital setting.

1. Introduction

In the year 2020, approximately 20 million new cases of cancer were registered worldwide, and one in 10 deaths can be attributed to cancer [1]. Every second cancer patient receives external beam radiation therapy [2], but the applicable dose and, thus, the treatment outcome is often limited by radiation-induced side effects to the surrounding organs at risk. One approach to overcome these limitations is microbeam radiation therapy (MRT), which is a form of spatially fractionated radiation therapy first explored by Slatkin et al. in 1992 [3]. With MRT, the X-ray field is modulated into 25–100 μm -thick planar beams spaced by 100–400 μm centre-to-centre distance. This dose modulation leads to a stripe pattern in the irradiated tissue

alternating between regions with doses up to several 100 Gy (called peaks) and regions only receiving scattered dose (called valleys) [4].

The microbeam pattern shows a peak-to-valley dose ratio (PVDR) that commonly ranges between 20 and 100 [5] and is facilitated by a tungsten multislit collimator in the X-ray beam [6]. Often, microbeam collimators consist of several stacked plates with individually wider slits shifted by a fraction of the slit width to circumvent manufacturing limitations [7,8]. Another approach for generating microbeams is by alternated stacking of foils of highly and little absorbing materials [9, 10], which, however, compromises the achievable PVDR. Numerous preclinical studies on MRT have been conducted both *in-vitro* and *in-vivo*, showing an enhanced differential effect with healthy tissue

* Corresponding author at: TUM School of Natural Sciences, Technical University of Munich (TUM), Garching, Germany.

E-mail address: ch.petrich@tum.de (C. Petrich).

¹ Shared first authorship.

tolerating unconventionally high peak doses and tumorous tissue being heavily damaged [11–14].

The X-ray source used for MRT needs to have a focal spot not larger than the slits of the collimator to limit the geometrical blur of the dose modulation on a micrometre scale. Additionally, energies in the orthovoltage regime are necessary to minimise the range of secondary electrons, allowing for steep beam penumbras while simultaneously reaching deeper seated tumours [5]. Furthermore, high dose rates are necessary for clinical applications to prevent blurring of the microbeam pattern due to organ motion [15]. The only radiation sources presently available fulfilling these requirements are 3rd-generation synchrotrons, which are, due to their large sizes and costs, unsuitable for clinical routine [5]. For preclinical experiments, other radiation sources have been employed, ranging from conventional X-ray tubes [16,17] to carbon nanotube sources [18] and inverse Compton scattering sources [19]. These preclinical microbeam sources lack sufficiently high energy, a sufficiently high dose rate, or a sufficiently small effective source spot for clinical MRT.

To overcome the limitations of the available compact X-ray sources for MRT, we designed and built the first prototype of a line-focus X-ray tube (LFXT). The LFXT is based on the rotating anode X-ray tube principle but is designed to be operated within the heat capacity limit [20]. The heat capacity limit enables the LFXT to reduce the focal spot width down to 50 μm and less without affecting the focal spot temperature. In the heat capacity limit, the focal spot temperature is mainly determined by the heat capacity of the target material, in contrast to conventional X-ray tubes, where the heat conductivity of the target material determines the focal spot temperature. That way, the LFXT is able to overcome the temperature limitations at the focal spot that conventional X-ray sources face and achieves the necessary beam characteristics for MRT. This enables the usage of high electron beam power focused on a very narrow focal spot. The LFXT prototype in our lab is designed to produce dose rates of more than 10 Gy/s at a water depth of 15 mm at a distance of 20 cm from the focal spot according to Monte Carlo simulations with a field size of 40 mm with an electron beam power of 90 kW focused into a 20 mm-long and 50 μm -wide focal spot [21,22].

Currently, we are in the process of commissioning the LFXT prototype. The generation of microbeams requires the formation of a narrow focal spot and a specialised multislit collimator forming the microbeam pattern. An essential step is the characterisation of the electron focal spot on the target in order to adjust the magnetic electron beam focusing. A sufficiently narrow focal spot, achieved by precise beam focusing, is required for a sharp microbeam dose profile behind the multislit collimator. Here, we report on two standard methods for characterising the X-ray focal spot that have been adapted to the requirements of the LFXT prototype, as well as the design of the microbeam collimator. The methods for focal spot characterisation and the collimator design are validated using Monte Carlo simulations.

2. Materials and methods

2.1. System overview of LFXT prototype

We designed the LFXT prototype for an electron beam current of 300 mA at a maximum acceleration voltage of 300 kV with the X-rays being emitted from a focal spot that is 50 μm wide and 20 mm long. For a future clinical version, acceleration voltages of up to 600 kV are planned, allowing the treatment of deeper seated target volumes. Lower voltages limit the penetration depth and thereby allow the treatment of target volumes close to the patient's surface. In Fig. 1, the LFXT prototype is shown with important components highlighted. The electron beam impinges onto the target parallel to the surface normal, and the primary X-ray beam is taken at an angle of 45° to the surface normal of the target.

The acceleration voltage and current are produced by two high-voltage generators delivering 300 mA each at ± 150 kV, respectively. Electrons are emitted from a thermionic cathode surrounded by a pierce electrode for beam control and primary focusing connected to the negative high-voltage source. The electron beam is accelerated towards a dedicated anode connected to the positive high-voltage source and passes through an elongated slit in the anode into the beam pipe. A series of magnets installed around the beam pipe focus the electron beam into its final shape on the target, where it impinges and creates X-ray photons. More information on the electron source and accelerator can be found in the publication by Matejcek et al. [23].

For operation in the heat capacity limit, the target of the LFXT prototype will rotate with a surface speed on the order of 200 m/s, causing both thermal stresses due to high temperature gradients in the material and mechanical stresses due to centrifugal force. The body of the target is made of a tungsten–zirconium–molybdenum alloy (TZM) with a diameter of 240 mm containing a 1 mm thick focal track made of a tungsten–rhenium alloy at the base of the cylindrical body. Detailed information on the target is given in the publication by Winter et al. [22].

2.2. Focal spot characterisation

Two approaches for imaging the focal spot of the LFXT prototype have been implemented. Adaptation of standardised approaches is necessary due to the extremely asymmetric and unconventionally large focal spot of the LFXT prototype combined with the 45° angle between the target surface, acting as the focal plane, and the X-ray beam axis.

We evaluate the performance of both approaches by Monte Carlo simulations assuming a rectangular, isotropic photon source. Both methods create an image of the focal spot with reduced resolution depending on the point spread function (PSF) of the method. Based on the simulated photon source, the obtained image and assuming a Gaussian PSF, the resolution is determined iteratively as the PSF full width at half maximum. The analysis and reconstruction procedures for both approaches are done using Python 3.

2.2.1. Pinhole method

One approach conventionally used to image the intensity distribution of the focal spot of an X-ray source utilises a so-called pinhole to form a camera obscura [24]. The pinhole is placed between the focal spot and the detector and consists of a highly absorbing plate with a very small aperture, allowing photons to pass. The main advantage of the pinhole method lies in its simplicity, as it yields a 2D representation of the focal spot within a single image without additional assumptions. However, the size of the pinhole is a trade-off between resolution and efficiency, and satisfactory signal-to-noise ratios often require long exposure times. Moreover, smaller pinholes need a higher angular alignment precision.

An analogue X-ray film can be used instead of a less resolving digital detector, limited only by the film grain size and the resolution of the scanner used for digitisation. On the resulting digital image, we apply the Richardson–Lucy-deconvolution algorithm [25,26] to reduce the influence of the pinhole and increase the resolution. Due to the large size of the focal spot and the angle between the beam axis and the focal plane of 45°, the size of the pinhole changes depending on the viewing angle. This leads to distortions in measured intensity and magnification that cannot be neglected. These distortions are corrected by approximating the visible aperture of the pinhole for each pixel. In the last step, the image is projected onto the source plane, resulting in a quantitative intensity distribution of the focal spot.

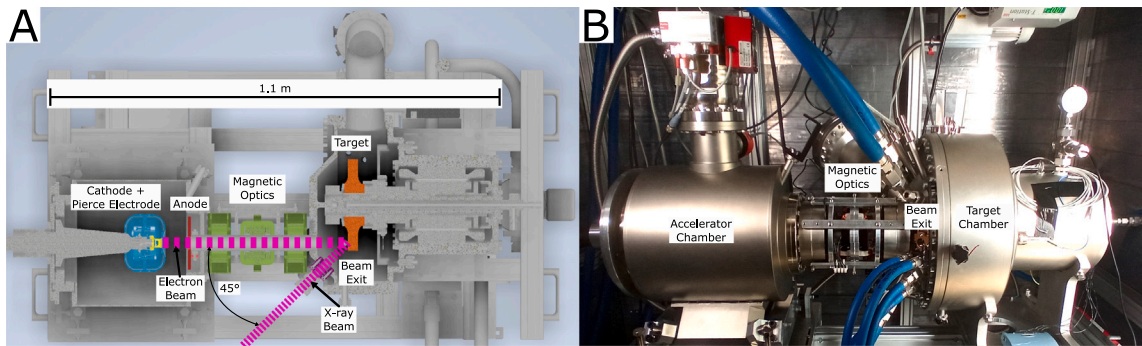


Fig. 1. A Horizontal cut (top view) through the CAD model of the LFXT prototype at the height of the electron and X-ray beam. On the left, the accelerator chamber with the cathode in yellow, the pierce electrode in blue, and the anode in red are shown, followed by the electron beam pipe surrounded by two quadrupoles and a dipole magnet in green. On the right is the target chamber with the target in orange and the primary beam exit in purple. The electron and X-ray beams are symbolised by thick magenta dashed lines with an angle of 45°. From left to right, the vacuum chamber has a size of 1.1 m. **B** Photograph of the assembled vacuum chamber inside the cabinet with the accelerator and target chamber, the magnetic optics and the beam exit labelled for orientation.

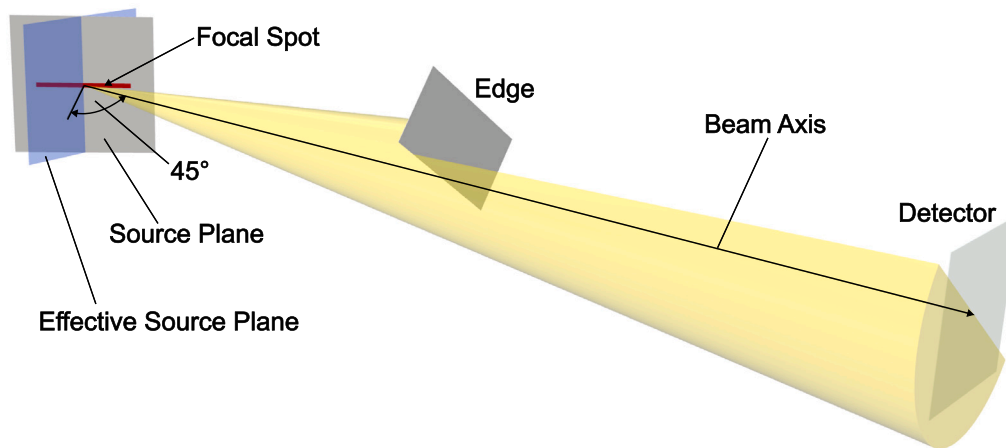


Fig. 2. Sketch of the measurement setup depicting the focal spot on the source plane, the effective source plane, an exemplary X-ray cone originating from the centre of the focal spot, the detector and the edge under an exemplary angle. For measurements and simulations of the pinhole method, the edge is exchanged for a pinhole.

2.2.2. Edge method

The second approach for measuring the intensity distribution of the focal spot of the LFXT prototype utilises a highly absorbing knife edge, as shown in Fig. 2 [27]. The one-dimensional derivative of the image on the X-ray detector perpendicular to the edge is the line spread function (LSF), which in turn is a line-integral projection of the focal spot. Therefore, the two-dimensional intensity distribution of the focal spot can be reconstructed similarly to computed tomography by acquiring projections under various edge angles. On the one hand, this method can achieve a very high resolution, which depends on the detector, the image statistics, and the number of projections. On the other hand, it requires a complex reconstruction and many projections, rendering it time-consuming. In the case of the LFXT prototype, it is necessary for reconstruction to assume that the source plane is parallel to the image plane. Projection from the assumed parallel source plane to the real source plane is done after reconstruction, see Fig. 2.

The first step in measuring the focal spot using the edge method is to acquire images under various angles of the edge rotated around the beam axis. Due to the highly asymmetric focal spot of the LFXT prototype, different geometrical magnifications are necessary for different angles to optimise resolution while fitting the magnified source into the field of view of the detector. The Nyquist frequency gives the number of necessary projections and depends on the resolution and size of the desired reconstruction field of view. As this can lead to a high number of images, a motorised stage for rotating the edge and a digital X-ray detector are highly favourable. Here, we assumed a photon-counting detector with 100 μm pixel size and box-like point spread

function (PSF). Filtered back-projection from Radon space to image space requires a uniform angular sampling of projections, leading to a high number of projections if a high resolution and a large field of view is required. To reduce the necessary number of projections, anisotropic pixels with different sizes of 100 μm in horizontal and 1 μm in vertical direction are defined during reconstruction for a 30.0 \times 0.2 mm^2 field of view (reconstruction space). Angular sampling for the Radon transform is done uniformly within reconstruction space using the corresponding Radon projections in real space. Hence, all projections contain an equal amount of information for the reconstruction, but sampling within real space is highly non-uniform.

In the second step, each image needs to be processed individually, starting with finding the precise position and angle of the edge in the image. With the geometry of the edge known, the pixels are sorted according to their distance perpendicular to the edge, resulting in a low-resolution edge spread function (ESF). Next, we apply an iterative back projection algorithm [28] adapted for one-dimensional data on a non-regular grid to get the high-resolution ESF. The algorithm intrinsically samples onto a regular grid and reduces noise. Additionally, we apply a Gaussian filter to reduce the noise of the high-resolution ESFs further and enable derivation of the LSF. Finally, the individual LSFs are geometrically projected onto the effective source plane.

After gathering all individual LSFs, we use the simultaneous algebraic reconstruction technique (SART) [29] for parallel beam geometry to reconstruct the effective focal spot. As mentioned before, we assume anisotropic pixels within the reconstruction space to reduce the

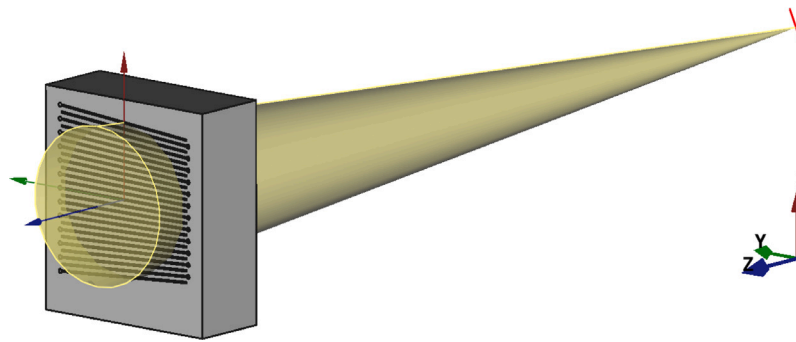


Fig. 3. Sketch of the collimator with the focal spot in red. The collimator slits are shown broader and fewer in number for clarity. The cone represents an exemplary X-ray beam originating from the centre of the focal spot.

necessary number of projections. For this, the individual LSFs need to be scaled according to the size of the respective reconstruction pixel, depending on the projection angle and intensity, due to the angle-dependent length of the projection path. The reconstructed effective focal spot must then be projected from the reconstruction plane, which is parallel to the detector plane, to the real focal plane tilted by 45° . For this step, it is necessary to assume that all projections have been acquired with the same geometrical magnification. The projection onto the focal plane then yields the quantitative spatial intensity distribution of the focal spot X-ray intensity.

2.3. Microbeam collimator for LFXT prototype

The microbeam collimator was made of a solid body with slits allowing the microbeams to pass. The requirements for the collimator resulted from the desired dose profile as well as the geometry of the LFXT prototype: The microbeams should have a width of $60\ \mu\text{m}$ and a centre-to-centre distance of $480\ \mu\text{m}$ at the target distance of $162.5\ \text{mm}$ from the focal spot. To maximise the achievable dose rate in the target, the collimator position should be as close to the beam exit window as possible, where the outer surface of the flange has a distance of $116.5\ \text{mm}$ from the focal spot. The leakage radiation should be below 0.025% of the primary X-radiation with a $300\ \text{kVp}$ spectrum from a tungsten target, which we calculated with the energy-dependent mass energy absorption coefficients. The rectangular field size should cover the entire beam that passes through the beam exit window with a diameter of the clear aperture of $16\ \text{mm}$ at $109.6\ \text{mm}$ from the focal spot. The compact X-ray source provides a divergent beam, to which the divergence of the slits had to be adapted based on the distance between the collimator and the focal spot. Also, the angle of 45° between the focal spot plane and the beam axis, see Fig. 2, had to be incorporated into the collimator design as tilt angles of the slits.

These requirements led to a collimator position (defined at rear side of the collimator, facing the sample) of $135\ \text{mm}$ from the focal spot and a field size of $20\ \text{mm}$ in x-direction and y-direction. The coordinate system of the collimator is shown in Fig. 3. The slit length in y-direction equalled the field size of $20\ \text{mm}$. In x-direction, the slit width was $50\ \mu\text{m}$ and the slit spacing was $400\ \mu\text{m}$ (defined at the rear side of the collimator), resulting in a total of 49 slits. The slits had to follow the microbeam planes. These microbeam planes were defined by the focal spot axis and by one additional point for each slit at the collimator rear surface: the centre of the field size in the y-direction with a spacing of $400\ \mu\text{m}$ in the x-direction. The focal spot axis was defined as $(0, -1/\sqrt{2}, 1/\sqrt{2})$. The angle of a specific slit was calculated by a rotation matrix around this focal spot axis. The rotation angle α of a specific slit was calculated as $\alpha = -\arctan(x \cdot \sqrt{2}/d)$, where x was the x-position of the slit, varied by the centre-to-centre distance between adjacent slits, and d was the distance between the collimator rear side and the focal spot.

Tungsten was chosen as the main collimator material for sufficient X-ray absorption. Due to higher manufacturing precision, the collimator body was made of Densimet[®], which consists of tungsten with nickel and iron added by a minor percentage. The centre plate of the collimator body had a thickness of $7\ \text{mm}$, both outer plates a thickness of $3.5\ \text{mm}$. The slits were manufactured by electrical discharge wire erosion (Seemann GmbH & Co. KG, Kirchenthumbach, Germany), which limited the slit width to a minimum of $120\ \mu\text{m}$. For this reason, a design of three layers was chosen with the centre plate shifted so that the actual slit width could be wider than $50\ \mu\text{m}$, similar to the collimator presented by Treibel et al. [8]. A shift of the centre plate by $71\ \mu\text{m}$ led to an effective slit width of $50\ \mu\text{m}$. Inserting the wire required a hole with a diameter of $170\ \mu\text{m}$ at one side of each slit. Pins ensured a fixed shift between the collimator plates.

The space restrictions required a compact design of the collimator and its holder as well as an off-centred location of the slits in the collimator body. The collimator body had a size of $28\ \text{mm}$ in x-direction, $25\ \text{mm}$ in y-direction and a total thickness of $14\ \text{mm}$ in z-direction. The collimator was modelled with FreeCAD (<https://www.freecad.org,version0.21.2>) and its Python console. The resulting model and a photograph of the collimator can be seen in Fig. 4.

2.4. Monte Carlo simulations

To validate the design of the microbeam collimator and the approaches for measuring the intensity distribution of the focal spot of the LFXT prototype, Monte Carlo simulations using TOPAS (version 3.9) [30] have been performed.

2.4.1. Pinhole

For the simulations of the pinhole method, a rectangular X-ray source with a length of $20\ \text{mm}$, a width of $50\ \mu\text{m}$, a flat intensity distribution and isotropic emission of $100\ \text{keV}$ mono-energetic X-ray photons was used. The X-ray energy was chosen to fit the mean energy of the LFXT prototype at $300\ \text{kVp}$. The normal vector of the source was tilted towards the beam axis by 45° . The pinhole was modelled as a $1\ \text{mm}$ thick tungsten plate with a hole of $25\ \mu\text{m}$, $50\ \mu\text{m}$, or $100\ \mu\text{m}$ diameter. Additionally, we conducted a simulation of an ideal pinhole with an infinitesimal small aperture in a fully absorbing infinitely thin plate. Scoring was done using a pixelated detector with a pixel size of $2.54\ \mu\text{m}$, imitating film resolution, and a field of view of about $2.5 \times 2.5\ \text{cm}^2$. The detector was placed $150\ \text{cm}$ from the centre of the focal spot, and the pinhole in the centre between them at $75\ \text{cm}$ from the focal spot. To reduce simulation time, we used phase-space sampling by only generating photons in a cone facing the pinhole from every point of the source. The cone was chosen to be large enough to fully illuminate the aperture of the pinhole and a part of the surrounding material from all angles. For each image, between 10^9 and 10^{10} photons were simulated to yield a low noise level. Simulations were performed using the physics list “g4em-penelope” with default parameters.

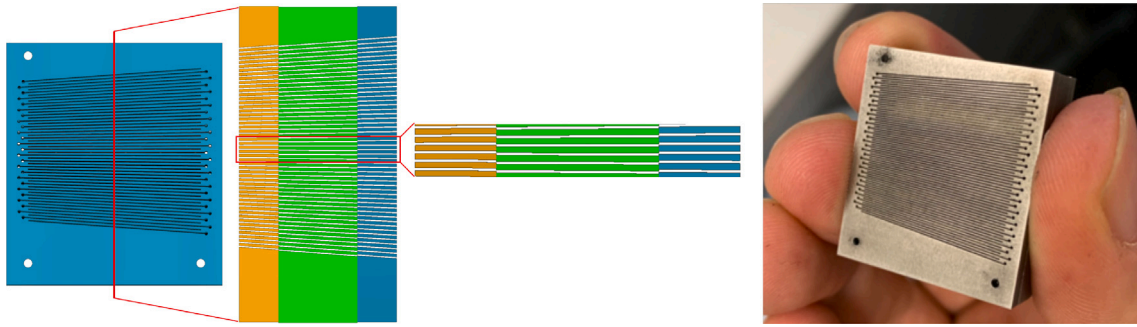


Fig. 4. Model (left) and photograph (right) of the microbeam collimator. The model is shown as a top view, as a central cut and a zoom thereof (from left to right). The collimator is composed of three layers, coloured orange, green and blue in the model, where the centre layer is shifted to achieve a smaller effective slit width than possible by manufacturing. Pins through the holes ensure the fixed shift of the three plates.

2.4.2. Edge

For the simulations of the edge method, the same rectangular X-ray source as for the pinhole simulations was used. The edge was modelled as a 1 mm thick tungsten plate and the pixelated detector with 100 μm pixel size and a field-of-view of $2.5 \times 2.5 \text{ cm}^2$. The distance between the focal spot and the detector was 150 cm. The edge was placed such that the ESF covered half of the detector, and about 800 projections were simulated. For each projection, 10^9 photons were generated. The distance of the edge to the source was adapted to the angle for each projection varying between 12 cm and 75 cm such that the geometrically magnified source always had an optimal size on the detector, with magnifications varying from 1.0 to 11.5. To reduce simulation time, we used phase-space sampling similar to the simulations for the pinhole method by aiming in a narrow cone at the centre of the detector. The diameter of the cone was chosen to be large enough to fully illuminate the detector from all angles. In addition to the simulations used for reconstructing the two-dimensional focal spot, simulations with $5 \cdot 10^{10}$ photons have been carried out with the edge vertically and horizontally aligned to get the respective LSFs with higher signal-to-noise ratio for comparison. As for the pinhole, simulations were performed using the physics list “g4em-penelope” with default parameters.

2.4.3. Collimator

The dose distribution behind the microbeam collimator was investigated using the physics list “g4em-penelope” with a minimum-energy cut-off of 100 eV and fluorescence, Auger electrons and particle-induced X-ray emission activated.

The photon source consisted of $1 \cdot 10^8$ primary particles, randomly distributed in a rectangle with a width of 50 μm and a length of 20 mm. The photon directions were randomly distributed around the positive z-direction with divergence-angle limitations to cover the field size of the collimator. The source was orientated along the axis defined by $(0, -1/\sqrt{2}, 1/\sqrt{2})$, as sketched in Fig. 3. The energy distribution was set according to a separately simulated 300 kVp X-ray spectrum from a tungsten target. As a comparison, additional simulations were performed using a point source with otherwise identical characteristics.

The photons travelled through 108 mm of vacuum, corresponding to the distance between the focal spot and the X-ray exit window, before entering air and hitting the microbeam collimator, which had a distance of 130 mm (rear / sample side of collimator) to the focal spot. The collimator plate consisted of pure tungsten with a thickness of 10 mm as a conservative estimate of the absorption. The field size was 20 mm \times 20 mm, and the slits were made of air and had divergence angles and tilt angles as described in Section 2.3. Additional simulations were performed using a collimator with parallel slits in the x-y-plane, i.e., considering the divergence of the beam but not the tilt angles resulting from the viewing angle of 45° onto the focal spot.

With an air gap of 10 mm behind the collimator, a water phantom was positioned to detect the dose-to-medium. The phantom had a size

of $30 \times 30 \times 50 \text{ mm}^3$ ($x \times y \times z$) and was divided into voxels with a size of $0.005 \times 1 \times 1 \text{ mm}^3$ ($x \times y \times z$). Between the collimator and the phantom, the phase space was detected and used ten times as a particle source in a second simulation for variance reduction.

The detected dose distribution was analysed with Python 3. Peak-valley-dose profiles (along the x-direction) were analysed for each depth in the water phantom at the centre ($y = 15 \text{ mm}$) of the field. The value of the detected peak voxels was averaged to obtain the individual peak dose. Valleys were defined as 60% of the difference between the distance of adjacent peaks and the peak width, where the distance of adjacent peaks was calculated according to the beam divergence. PVDR values were obtained for each peak position and then averaged over all peak positions at a specific depth.

3. Results

3.1. Simulations of focal spot measurement

3.1.1. Pinhole method

The results from the pinhole simulations are presented in Fig. 5. In Fig. 5B, all realistic pinholes yield a similar resolution of approximately 18 μm FWHM. For comparison, the simulation with the ideal, infinitely small pinhole is shown. The applied Richardson–Lucy deconvolution algorithm is not converging but instead compressing and distorting the small dimension of the simulated focal spot if a too high number of iterations is applied. In Fig. 5D, minor artefacts in the form of peaks at the ends of the focal spot can be seen. These are standard artefacts produced by the Richardson–Lucy deconvolution algorithm at edges. By comparing the results achieved with an ideal pinhole presented in Fig. 5A to those achieved with a realistic 100 μm pinhole presented in Fig. 5C, it can be seen that the realistic pinhole leads to a loss of resolution and quantitative validity but is able to yield a rough representation of the focal spot.

Although the applied corrections for distortions in intensity and dimension are working well, the resolution of the pinhole approach is insufficient for measuring the original rectangular shape of the focal spot with a width of 50 μm quantitatively.

3.1.2. Edge method

Fig. 6 shows the focal spot reconstruction from the simulations using a tungsten edge. In Fig. 6A, the focal spot reconstructed from the simulated projections exhibits an approximately homogeneous intensity distribution and reliably represents the original source used for the simulations. Minor artefacts arising from the reconstruction are visible, especially at the left and right ends of the focal spot. Across the long horizontal dimension, the reconstructed focal spot exhibits an approximately linear intensity gradient of about $\pm 11\%$ due to the varying distance of the focal spot to the detector.

In Figs. 6B and 6C, the LSFs calculated by summing up the reconstructed focal spot along its horizontal and vertical axes are compared

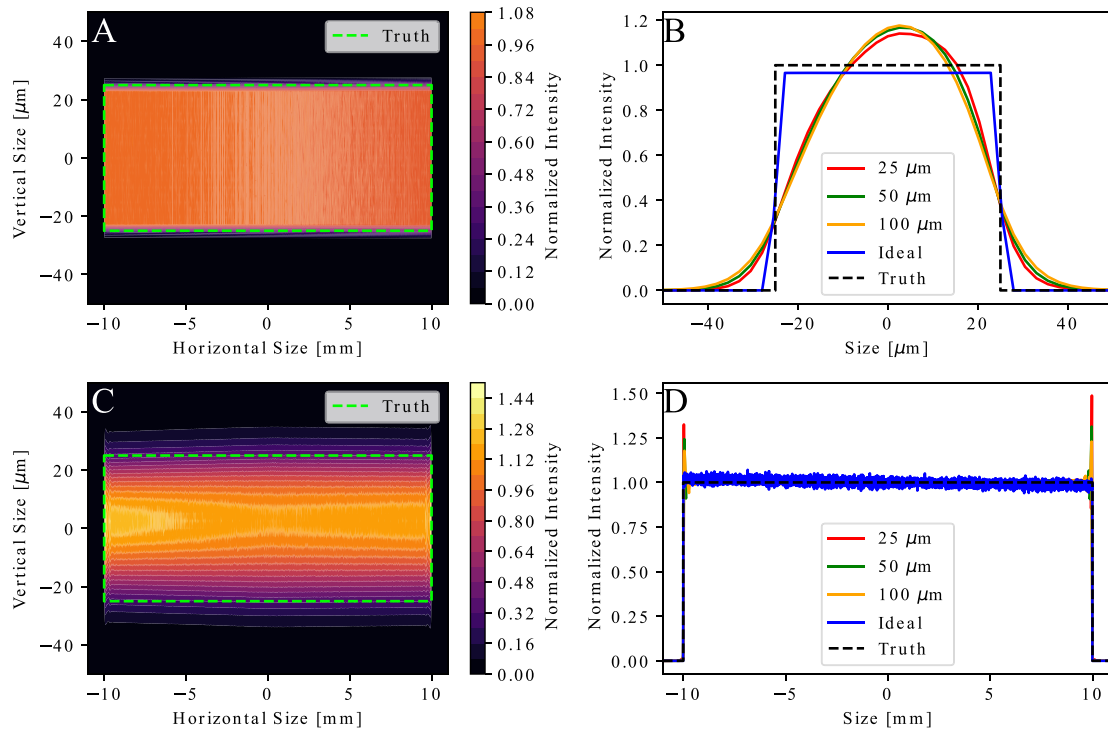


Fig. 5. Results of simulated pinhole measurements. In A and C, the resulting two-dimensional intensity distributions of the focal spot from simulations with the ideal and the 100 μm wide pinholes are shown. In green, the outline of the ground truth is shown where the intensity outside should be zero and inside homogeneous. Both images share the same colour scale. In B, the vertical and in D, the horizontal line spread functions (LSFs) are shown for different pinhole sizes of 25 μm , 50 μm , and 100 μm together with the results for the ideal pinhole and the ground truth. Shown intensities are normalised to ground truth.

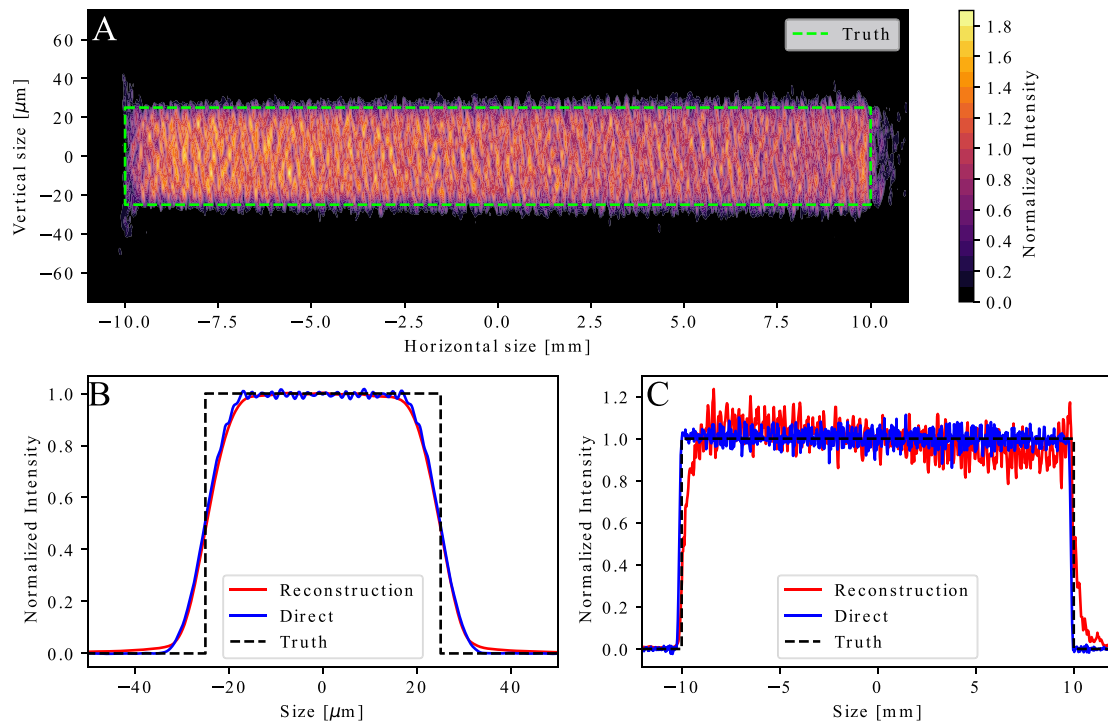


Fig. 6. Results of simulated edge measurement. In A, the focal spot reconstructed from the simulated edge projections is shown. In green, the outline of the ground truth is registered where the intensity outside should be zero and inside homogeneous. In B and C, the vertical and horizontal line-spread functions (LSFs), as calculated from the reconstructed focal spot and as directly measured with the edge, are shown for comparison. Shown intensities are normalised to ground truth.

to the ground truth and to LSFs directly measured using the edge. As the directly measured LSFs were simulated with higher statistics, a smaller Gaussian filter could be used in the derivation step. The vertical LSF calculated from the reconstructed focal spot and the directly measured

vertical LSF show no considerable difference. From this, we conclude that the resolution of the reconstructed focal spot is not limited by the filter applied for deriving the ESF but rather by the resolution of the detector itself and by scattering within the material of the edge.

Overall, the box-like shape of the focal spot can be well approximated by the edge method, achieving a resolution of about 9 μm FWHM.

3.2. Simulations for microbeam collimator

The developed collimator with divergent and tilted slits resulted in a sharp microbeam dose distribution, as presented in Fig. 7A. Dose profiles acquired with the extended LFXT source and the point source agreed within their simulation uncertainties, which were represented as standard deviations of the peak width, the peak and valley doses, and the PVDR. A comparison between these two dose profiles at the surface of the phantom is exemplary shown in Fig. 7A and 7B. For the extended source, the mean PVDR across the microbeam field was 122 ± 21 at the surface, 30 ± 4 at a water depth of 10 mm, and stayed above 23 throughout the entire water phantom of a thickness of 50 mm, as depicted in Fig. 7D. At the surface of the phantom, the peak dose and PVDR decreased, while the peak width increased with lateral distance to the central beam axis (z-axis). The central peak width (as FWHM) was 53.1 ± 0.9 μm at the phantom surface and showed an increasing trend with depth due to photon scattering and field divergence. The mean centre-to-centre distance between neighbouring peaks showed an increasing trend from 434 ± 13 μm to 583 ± 20 μm mainly due to the divergence of the radiation field.

Only for the point source, the collimator with parallel slits in the x–y-plane resulted in a similar dose profile as the collimator with tilted slits. The combination of the extended LFXT source and the collimator with parallel slits led to a strong decrease of the peak dose with increased distance from the central beam axis at all depths, shown in Fig. 7C. For the extended LFXT source, the peak dose obtained with the collimator with tilted slits showed a reduction by a factor of 2 from the field centre to the field edge, while the peak dose obtained with the collimator with parallel slits showed a reduction by a factor of 3, both acquired at the phantom surface. For the collimator with parallel slits, the decreased peak dose resulted in a decreased mean PVDR of 96 ± 28 at the surface of the phantom, 21 ± 8 at 10 mm depth and 11 ± 8 at 40 mm depth.

4. Discussion

4.1. Comparison of focal spot measurement methods

Both methods for measuring the focal spot, whether using a pinhole or an edge, yield a qualitative image of the source spot. The pinhole method enables the visualisation of the focal spot within a single image acquisition and without complex reconstruction methods but is limited in resolution by the size of the aperture of the used pinhole. The applied Richardson–Lucy deconvolution algorithm has been shown to diminish the quantitative validity of the measured focal spot and is, therefore, unsuitable for quantitative measurements of the focal spot width. Other deconvolution methods, such as Gold’s ratio method or relaxation-based methods [31], could be tested to potentially enhance the resolution of the pinhole approach without diminishing quantitative validity. The usage of smaller pinhole apertures has practical limitations, e.g. due to necessary measurement time, positioning accuracy, and viewing angle-dependent artefacts.

The edge method requires an elaborate and laborious measurement setup and procedure, including a high number of image acquisitions, rendering it highly time-consuming, followed by a complex analysis and reconstruction workflow. Nevertheless, the edge method has been shown to be able to yield a representation of the simulated focal spot with a resolution of approximately 9 μm FWHM and high quantitative validity. Additionally, the resolution achievable with the edge method could be further improved by using a higher resolving detector and by increasing the number of acquired projections according to the Nyquist criterion [32].

We will use the pinhole method as a quick approach for visualising the focal spot of the LFXT prototype during the commissioning process for adjusting the settings of the electron beam optics. The edge method is the superior approach, both concerning resolution and quantitative validity and will be used once the commissioning of the LFXT prototype has been concluded and the machine parameters have been adjusted. The latter method allows accurate X-ray source characterisation for Monte Carlo modelling, dose prediction and treatment planning. Aside from application to the LFXT prototype and future clinical LFXT versions, the presented results for the focal spot measurement methods can be applied to any X-ray source, especially to X-ray sources with asymmetric focal spots.

4.2. Microbeam collimator

The collimator with divergent and tilted slits can produce a sharp peak–valley dose profile with a PVDR of 30 at a water depth of 10 mm suitable for preclinical MRT. The achievable microbeam dose distribution at the presented small field size is better suited for *in vivo* studies with target volumes at a few centimetres depth in tissue than other compact microbeam sources [17] due to the considerably higher PVDR throughout 50 mm of water of the LFXT. Clinical MRT will require field sizes of 5–10 mm or potentially even larger, which involves lower PVDR values due to a higher amount of scattered radiation. For the design of the clinically applicable LFXT version, relevant effects of the photon spectrum and the field size on the PVDR will be considered. The ideal dose profile for clinical MRT, including the ideal PVDR, is currently a topic of scientific discussion [5].

The extended photon source and the angle between the target surface and the X-ray beam axis demand the complex collimator geometry with divergence and tilt angles of the slits. This demand was demonstrated by additionally simulating parallel slits (in the x–y-plane), leading to a distorted microbeam dose profile. Due to the fixed slit angles, the collimator with tilted slits needs to be positioned at the predefined distance from the focal spot at an angle of 45° to the target surface with a sub-millimetre translational and sub-degree rotational alignment precision. To achieve this alignment precision, the collimator will be mounted into a movable holder for translation and rotation adjustments. The rotational alignment has to include an angular adjustment around the normal to its surface, in contrast to the collimator presented by Treibel et al. [8]. The collimator alignment depends only on the source geometry, not on the individual patient positioning. Therefore, the collimator must be aligned only once after mounting, followed by regular constancy checks.

A limitation of the simulations was the size of scoring voxels of 1 mm in y-direction and z-direction. Due to the divergence of the beam and the extension of the source in both of these directions, partial volume effects led to a decreased dose and an increased width for off-centre peaks, which was stronger the larger the distance to the central axis. Another minor reason for the decreased peak dose and increased peak width at the periphery of the field was the divergence of the beam, as the distance to the source was larger for locations on the periphery of the field than at the centre. For a simulation of more precise dose distributions, the size of the scoring voxels would need to be drastically reduced to achieve a micrometre resolution in all three dimensions. However, a reduction from 1 mm to 5 μm in y-direction and z-direction would lead to a decrease in signal-to-noise ratio of a factor of 40,000. Longer simulation times to compensate by this factor would not be reasonable. More importantly, the comparison between the extended LFXT source and the point source did not show relevant differences in the dose distribution, which leads to the conclusion that the collimator design matches the characteristics of the focal spot of the LFXT.

The presented preclinical LFXT will deliver microbeam field sizes of 20 mm \times 20 mm suitable for cell experiments and preclinical studies with small rodents. In contrast, a clinically applicable LFXT will require larger field sizes to cover clinical target volumes. Large microbeam field

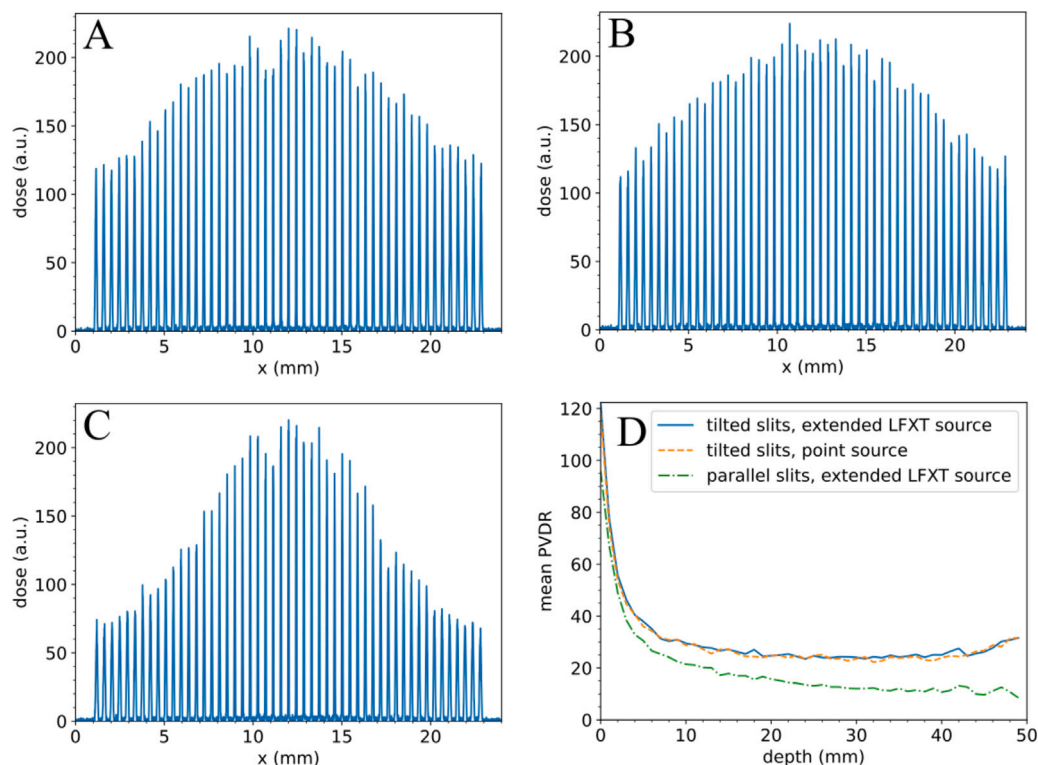


Fig. 7. Microbeam dose profile at the centre of the radiation field ($y=15$ mm) at the surface of the water phantom for the collimator with tilted slits and the extended LFXT source in A, for the collimator with tilted slits and the point source in B and for the collimator with parallel slits and the extended LFXT source in C. In D, the peak-to-valley-dose ratio (PVDR) in the water phantom is averaged over all peaks at each depth.

sizes pose a challenge in the manufacturing of the multislit collimator and involve a trade-off with lower PVDRs. Despite high dose rates, motion mitigation techniques will be necessary depending on the irradiated body region. Preclinical irradiations of, e.g., the lung, at the presented LFXT prototype will require breathing gating, which is possible by fast switching of the electron beam [23]. Clinical microbeam treatments will involve gating regarding breathing and possibly the heartbeat.

5. Conclusions

In this work, there are two approaches for measuring the focal spot of an X-ray source adapted to the specific requirements of the LFXT prototype presented and validated using Monte Carlo simulations. We showed that the pinhole method can be used to visualise the approximate shape and size of the focal spot of the LFXT prototype but lacks resolution and quantitative validity. The adapted edge method, although significantly more complex and labour-intensive, can provide a quantitative representation of the focal spot of the LFXT prototype with a resolution of approximately $9 \mu\text{m}$. During the commissioning process of the LFXT prototype, the pinhole method will be used as an easy-to-use way of visualising the focal spot during the adjustment of the electron beam and as an initial characterisation of the X-ray focal spot. For a quantitative characterisation, the edge method will be used in a second step.

After adjustment of the focal spot through the aforementioned methods, the microbeam collimator can be used to produce the desired microbeam dose profile. We demonstrated that the LFXT source requires a dedicated collimator geometry accounting for divergence and tilt angles. The presented collimator design is able to produce a microbeam dose profile with approximately $53.1 \pm 0.9 \mu\text{m}$ -wide peaks spaced by $434 \pm 13 \mu\text{m}$. In simulations, a PVDR of 30 was achieved in a depth of 10 mm within a water phantom and remained above 23 over the full 50 mm deep phantom.

Once the commissioning of the LFXT prototype is completed, *in vitro* and *in vivo* studies will soon be carried out. The experience of this LFXT prototype will guide the design of a clinical machine, which will likely facilitate the first clinical trials with MRT.

Declaration of competing interest

The authors declare that they have no competing financial interests or personal relationships that could have appeared to influence the work reported in this paper.

Acknowledgements

This work was supported by the German Research Foundation (Deutsche Forschungsgemeinschaft) through the Emmy Noether Programme [grant number 416790481], the German Federal Ministry of Education and Research (BMBF) through the GoBio Programme [grant number 16LW0396] and the Innovation Fund at Forschungszentrum Jülich.

References

- [1] Ferlay J, Colombet M, Soerjomataram I, Parkin DM, Piñeros M, Znaor A, et al. Cancer statistics for the year 2020: An overview. *Int J Cancer* 2021;149(4):778–89. <http://dx.doi.org/10.1002/IJC.33588>.
- [2] Delaney G, Barton M. Evidence-based estimates of the demand for radiotherapy. *Clin Oncol* 2015;27(2):70–6. <http://dx.doi.org/10.1016/j.clon.2014.10.005>.
- [3] Slatkin DN, Spanne P, Dilmanian FA, Sandborg M. Microbeam radiation therapy. *Med Phys* 1992;19(6):1395–400. <http://dx.doi.org/10.1118/1.596771>.
- [4] Bräuer-Krisch E, Serduc R, Siegbahn E, Duc GL, Prezado Y, Bravin A, et al. Effects of pulsed, spatially fractionated, microscopic synchrotron X-ray beams on normal and tumoral brain tissue. *Mutation Res/Rev Mutation Res* 2010;704(1–3):160–6. <http://dx.doi.org/10.1016/j.mrrev.2009.12.003>.
- [5] Bartzsch S, Corde S, Crosbie JC, Day L, Donzelli M, Krusch M, et al. Technical advances in x-ray microbeam radiation therapy. *Phys Med Biol* 2020;65(2):02TR01. <http://dx.doi.org/10.1088/1361-6560/AB5507>.

- [6] Pelliccioli P, Donzelli M, Davis JA, Estève F, Hugtenburg R, Guatelli S, et al. Study of the X-ray radiation interaction with a multislit collimator for the creation of microbeams in radiation therapy. *J Synchrotron Radiat* 2021;28(2):392–403. <http://dx.doi.org/10.1107/S1600577520016811>.
- [7] Bräuer-Krisch E, Requardt H, Brochard T, Berruyer G, Renier M, Laissue JA, et al. New technology enables high precision multislit collimators for microbeam radiation therapy. *Rev Sci Instrum* 2009;80(7):74301. <http://dx.doi.org/10.1063/1.3170035/352070>.
- [8] Treibel F, Nguyen M, Ahmed M, Dombrowsky A, Wilkens JJ, Combs SE, et al. Establishment of microbeam radiation therapy at a small-animal irradiator. *Int J Radiat Oncol Biol Phys* 2021;109(2):626–36. <http://dx.doi.org/10.1016/j.ijrobp.2020.09.039>.
- [9] Slatkin DN, Dilmanian FA, Nawrocky MM, Spanne P, Gebbers J-O, Archer DW, et al. Design of a multislit, variable width collimator for microplanar beam radiotherapy. *Rev Sci Instrum* 1995;66(2):1459–60. <http://dx.doi.org/10.1063/1.1145940>.
- [10] Stengl C, Arbes E, Thai LYJ, Echner G, Vedelago J, Jansen J, et al. Development and characterization of a versatile mini-beam collimator for pre-clinical photon beam irradiation. *Med Phys* 2023;50(8):5222–37. <http://dx.doi.org/10.1002/MP.16432>.
- [11] Smyth LM, Rogers PAW, Crosbie JC, Donoghue JF. Characterization of diffuse intrinsic pontine glioma radiosensitivity using synchrotron microbeam radiotherapy and conventional radiation therapy in vitro. *Radiat Res* 2018;189(2):146–55. <http://dx.doi.org/10.1667/RR4633.1>.
- [12] Laissue J, Blattmann H, Wagner HP, Grotzer MA, Slatkin DN. Prospects for microbeam radiation therapy of brain tumours in children to reduce neurological sequelae. *Dev Med Child Neurol* 2007;49(8):577–81. <http://dx.doi.org/10.1111/j.1469-8749.2007.00577.x>.
- [13] Bouchet A, Bräuer-Krisch E, Prezado Y, Atifi ME, Rogalev L, Clec'h CL, et al. Better efficacy of synchrotron spatially microfractionated radiation therapy than uniform radiation therapy on glioma. *Int J Radiat Oncol Biol Phys* 2016;95(5):1485–94. <http://dx.doi.org/10.1016/j.ijrobp.2016.03.040>.
- [14] Crosbie JC, Anderson RL, Rothkamm K, Restall CM, Cann L, Ruwanpura S, et al. Tumor cell response to synchrotron microbeam radiation therapy differs markedly from cells in normal tissues. *Int J Radiat Oncol Biol Phys* 2010;77(3):886–94. <http://dx.doi.org/10.1016/j.ijrobp.2010.01.035>.
- [15] Winter J, Galek M, Matejcek C, Wilkens JJ, Aulenbacher K, Combs SE, et al. Clinical microbeam radiation therapy with a compact source: specifications of the line-focus X-ray tube. *Phys Imaging Radiat Oncol* 2020;14:74–81. <http://dx.doi.org/10.1016/j.phro.2020.05.010>.
- [16] Bartzsch S, Cummings C, Eismann S, Oelfke U. A preclinical microbeam facility with a conventional x-ray tube. *Med Phys* 2016;43(12):6301–8. <http://dx.doi.org/10.1118/1.4966032>.
- [17] Ahmed M, Bicher S, Combs SE, Lindner R, Raulefs S, Schmid TE, et al. In vivo microbeam radiation therapy at a conventional small animal irradiator. *Cancers* 2024;16(3):581. <http://dx.doi.org/10.3390/cancers16030581>.
- [18] Hadsell M, Zhang J, Laganis P, Sprenger F, Shan J, Zhang L, et al. A first generation compact microbeam radiation therapy system based on carbon nanotube X-ray technology. *Appl Phys Lett* 2013;103(18):183505. <http://dx.doi.org/10.1063/1.4826587>.
- [19] Burger K, Urban T, Dombrowsky AC, Dierolf M, Günther B, Bartzsch S, et al. Technical and dosimetric realization of in vivo x-ray microbeam irradiations at the munich compact light source. *Med Phys* 2020;47(10):5183–93. <http://dx.doi.org/10.1002/mp.14433>.
- [20] Bartzsch S, Oelfke U. Line focus x-ray tubes—a new concept to produce high brilliance x-rays. *Phys Med Biol* 2017;62(22):8600–15. <http://dx.doi.org/10.1088/1361-6560/aa910b>.
- [21] Winter J. Microbeam radiotherapy on the path to clinical application: A powerful compact x-ray source and microbeam treatment planning. 2023, <https://nbn-resolving.de/urn/resolver.pl?urn:nbn:de:bvb:91-diss-20230419-1687953-1-7>.
- [22] Winter J, Dimroth A, Roetzer S, Zhang Y, Krämer KL, Petrich C, et al. Heat management of a compact x-ray source for microbeam radiotherapy and FLASH treatments. *Med Phys* 2022;49(5):3375–88. <http://dx.doi.org/10.1002/MP.15611>.
- [23] Matejcek C, Winter J, Aulenbacher K, Dimroth A, Natour G, Bartzsch S. A novel electron source for a compact x-ray tube for microbeam radiotherapy with very high dose rates. *Phys Medica* 2023;106:102532. <http://dx.doi.org/10.1016/j.ejmp.2023.102532>.
- [24] DIN German Institute for Standardization. DIN EN 12543-2: Non-destructive testing - characteristics of focal spots in industrial X-ray systems for use in non-destructive testing - part 2: Pinhole camera radiographic method. 2021.
- [25] Richardson WH. Bayesian-based iterative method of image restoration*. *J Opt Soc Am* 1972;62(1):55. <http://dx.doi.org/10.1364/JOSA.62.000055>.
- [26] Lucy L. An iterative technique for the rectification of observed distributions. *Astron J* 1974;79(6):745. <http://dx.doi.org/10.1086/111605>.
- [27] DIN German Institute for Standardization. DIN EN 12543-4: Non-destructive testing - characteristics of focal spots in industrial X-ray systems for use in non-destructive testing - part 4: Edge method. 1999.
- [28] Park SC, Park MK, Kang MG. Super-resolution image reconstruction: a technical overview. *IEEE Signal Process Mag* 2003;20(3):21–36. <http://dx.doi.org/10.1109/MSP.2003.1203207>.
- [29] Andersen A. Simultaneous algebraic reconstruction technique (SART): A superior implementation of the ART algorithm. *Ultrason Imaging* 1984;6(1):81–94. [http://dx.doi.org/10.1016/0161-7346\(84\)90008-7](http://dx.doi.org/10.1016/0161-7346(84)90008-7).
- [30] Faddegon B, Ramos-Méndez J, Schuemann J, McNamara A, Shin J, Perl J, et al. The TOPAS tool for particle simulation, a Monte Carlo simulation tool for physics, biology and clinical research. *Phys Medica* 2020;72:114–21. <http://dx.doi.org/10.1016/j.ejmp.2020.03.019>.
- [31] Crilly P. A quantitative evaluation of various iterative deconvolution algorithms. *IEEE Trans Instrum Meas* 1991;40(3):558–62. <http://dx.doi.org/10.1109/19.87019>.
- [32] Zhu Z, Wahid K, Babyn P. CT image reconstruction from partial angular measurements via compressed sensing. In: 2012 25th IEEE Canadian conference on electrical and computer engineering (CCECE). 2012, p. 1–4. <http://dx.doi.org/10.1109/CCECE.2012.6334926>.